Ultrasound-Stimulated Vibro-Acoustic Spectrography

Mostafa Fatemi and James F. Greenleaf

An ultrasound method based on radiation force is presented for imaging the acoustic response of a material to mechanical excitation. Acoustic energy was emitted from solids and tissues in response to an oscillatory radiation force produced by interfering focused beams of ultrasound. Frequency spectra of ultrasound-stimulated acoustic emission exhibited object resonances. Raster-scanning the radiation force over the object and recording the amplitude and phase of the emitted sound resulted in data from which images related to the elastic compositions of the acoustically emitting objects could be computed. Acoustic emission signals distinguished tuning-fork resonances, submillimeter glass spheres, and calcification in excised arteries and detected object motions on the order of nanometers.

The mechanical response of objects to external forces is of considerable interest in medical diagnosis, nondestructive inspection of materials, and materials science. An applied force is often used to produce displacement from which elastic constants, like spring constants, can be determined. In resonant ultrasound spectroscopy, an ultrasound source and a detector are used to measure the resonance frequencies of a sample with known size and mass. The resonances are related to mechanical parameters, including the elastic constants of the material (*1*). Recently, a magnetic resonance elastography method for quantitatively measuring the displacement of tissues in response to externally applied cyclic forces was reported by Muthupillai *et al.* (*2*). The method resulted in high-resolution images of the shear modulus of normal and pathologic tissues. Others have used ultrasound to measure tissue displacement associated with externally applied compressive and cyclic forces (*3*).

We describe an imaging technique that uses acoustic emission to map the mechanical response of an object to local cyclic radiation forces produced by interfering ultrasound beams. Radiation force is generated by changes in the energy density of an acoustic field (*4*). For instance, a collimated ultrasound beam impinging normally on the surface of an object of arbitrary shape and boundary impedance will produce a radiation force. The radiation force arising from this interaction has a component $F = d_r s\langle E\rangle$ (*5*) in the beam direction. This component is proportional to the time-average energy density of the incident wave $\langle E\rangle$, the projected area of the object s, and d_r (*6*), the scattering and absorbing properties of the object.

We probe the object by arranging the intersection of two focused continuous-wave (CW) ultrasound beams of different frequencies at a selected point on the object. Interference in the intersection region of the two beams produces sinusoidal modulation of the ultrasound energy density. Modulation of the energy density creates an oscillatory force, effectively vibrating the object at the selected region. The resulting vibration of the object produces an acoustic field [acoustic emission (*7*)] that can be measured some distance away.

Ultrasound beams can be constructed in a variety of ways for this purpose (*8*). We used two coaxial, confocal transducer elements of a spherically focused annular array (consisting of a central disc and an outer annulus) driven by two CW signals at slightly different frequencies ω_1 and ω_2 (Fig. 1). The energy density at a point in this ultrasound field, say at the focus, is proportional to the square of the sum of the ultrasound fields from the two elements. Squaring the sum of two sines gives rise to sum and difference frequency terms. Thus, high-frequency and low-frequency variations in energy density result at the intersection of the two beams produced by the two elements. Ultrasound-stimulated acoustic emission results from the energy term that produces a low-frequency vibration. The low-frequency force on a target at the focal point can be computed by

$$F_l(t) = d_r \iint_S \langle E_{focal}(t,x,y)\rangle_T \, dxdy$$

$$= Cd_r \cos(\Delta\omega t) \qquad (1)$$

where C is a constant, $\Delta\omega = |\omega_1 - \omega_2|$, S is the area over which $E_{focal}(t,x,y)$, the total energy density in the focal plane, has significant value, and $\langle\rangle_T$ represents a short-term time average (*9*). For focused beams, the intersection region can be small enough that $F_l(t)$ can be considered to be an oscillating point force applied to the object at the focal intersection of the beams.

To produce an ultrasound-stimulated vibro-acoustic spectrogram, we vibrate a small region of the object with an oscillating radiation force of varying frequency. The complex amplitude of the resulting acoustic emission field is

$$\Phi(\Delta\omega) = Cd_r H(\Delta\omega)Q(\Delta\omega) \qquad (2)$$

where $Q(\Delta\omega)$ is a complex function representing the mechanical frequency response, or admittance, of the object at the selected point, and $H(\Delta\omega)$ represents the combined frequency response, or transfer function, of the propagation medium and receiver and is assumed to be fixed and known (*10*). Recording $\Phi(\Delta\omega)$ allows us to obtain $Q(\Delta\omega)$ for each point within a constant multiplier (*11*). We raster-scan the radiation force over the object to produce data, which can

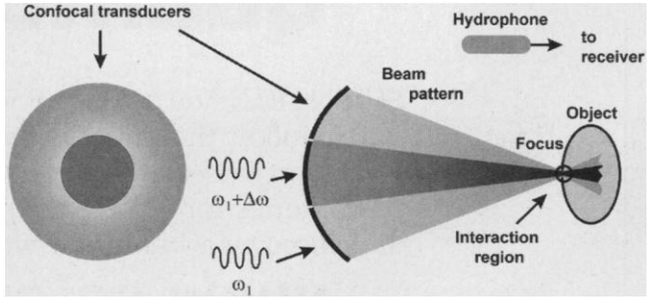

Fig. 1. Experimental system for ultrasound-stimulated vibro-acoustic spectrography: a two-element confocal ultrasound annular array transducer, consisting of a center disc and an outer ring. The elements are driven by two CW sources, at frequencies equal to ω_1 and $\omega_2 = \omega_1 + \Delta\omega$, where these frequencies are very close to the central frequency of the elements, and $\Delta\omega$ is much smaller than (<1%) the center frequency of the ultrasound transducer. The beams interact only in a small region around the joint focal point, where the amplitude of the field oscillates at the difference frequency $\Delta\omega$. The region of interest is placed at the joint focal point and is probed point-by-point by raster scanning. The sound field resulting from object vibrations at each position is received by a hydrophone and recorded. The recorded signal at one or more difference frequencies is used to form an image of the object. The experiments were conducted in a water tank. The transducer center frequency was 3 MHz; its outer diameter was 45 mm; and it was focused at 70 mm. The difference frequencies used in each experiment are mentioned in the corresponding legends.

Ultrasound Research, Department of Physiology and Biophysics, Mayo Clinic and Mayo Foundation, Rochester, MN 55905, USA.

be mapped into a pictorial format. The spatial resolution of the resulting image is determined by the region in which significant interference between the ultrasound beams occurs and is of the order of a few wavelengths at the ultrasound frequency.

Experiments were conducted in a water tank, which provided good ultrasonic and acoustic coupling to the object and freedom of movement for the prototype scanner mechanism (Fig. 1). The two-element confocal ultrasound transducer array was positioned such that the beams interfered at the selected region of the object. Sound produced by vibrations of the object is approximately omnidirectional because of the small size of the vibrating portion of the object compared with the wavelength. This sound was detected by a submerged hydrophone placed near the object within the water tank.

To test the hypothesis that ultrasound-stimulated acoustic emission is sensitive to object mechanical properties and to show how such properties can be quantitatively evaluated by this method, we produced an ultrasound-stimulated vibro-acoustic spectrogram of a tuning fork immersed in isopropyl alcohol at two different temperatures. We aimed the focal point of the confocal transducer at a fixed position on one of the tines. The shear viscosity of alcohol changes with temperature, causing a slight, but detectable, shift in the spectrogram (Fig. 2). The shear viscosity η of a liquid is determined by measuring the resonant frequency f_R and the bandwidth δf_R of a tuning fork immersed in this liquid (12)

$$\eta = \frac{\kappa f_R}{\rho}\left(\frac{\delta f_R}{f_R} - \frac{\delta f_{R0}}{f_{R0}}\right)^2 \qquad (3)$$

where f_{R0} and δf_{R0} are the resonant frequency and bandwidth measured in vacuum, respectively, and ρ is the liquid density. The constant κ is determined experimentally. The measured values for f_R and δf_R were 1769 and 5.76 Hz at 15°C and 1765.7 and 4.53 Hz at 30°C. The viscosity of isopropyl alcohol is reported to be 2.89 cP (1 centipoise = 1 mPa·s) at 15°C (*13*). From this value, the constant κ was calculated. The shear viscosity at 30°C was found using Eq. 3 to be η = 1.77 cP, which is the same as the published data (*13*).

We tested the ability of ultrasonically stimulated vibro-acoustic spectrography to image the frequency response of different objects with identical d_r by scanning three tuning forks with different resonant frequencies. A color acoustic spectrogram was obtained by sweeping the frequency of the radiation force, $\Delta\omega$, in a range covering the resonant frequencies of all forks at each beam position. The acoustic emission signal was filtered by three bandpass filters centered at different frequencies. The outputs of these filters were used to form a three-color composite image (Fig. 3). The forks appear with three distinct colors because each fork responds primarily at its own resonant frequency. Because the forks were made from identical materials, other ultrasound imaging methods would not be capable of distinguishing these objects.

We tested the hypothesis that the amplitude of acoustic emission at a single frequency can be used to detect small, highly reflective isolated objects. We scanned a 380-μm-diameter glass bead placed on a thin latex sheet and recorded the amplitude of acoustic emission (Fig. 4). The latex sheet produces only a small change in the incident energy because it is almost transparent to the ultrasound beam. This experiment demonstrated the ability of the method to detect isolated regions of hardness with respect to a soft background.

To test the feasibility of using the technique to image mechanical properties of tissues, we measured the phase and amplitude of acoustic emission from calcified and noncalcified excised human iliac arteries. The arteries were scanned in a plane perpendicular to the ultrasound beam axis.

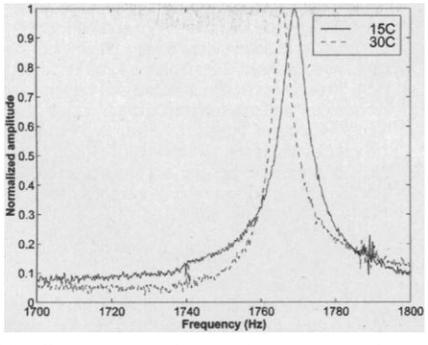

Fig. 2. Vibro-acoustic spectrograms of a tuning fork immersed in isopropyl alcohol at two different temperatures. A point on a tine of the fork was vibrated with the use of the system shown in Fig. 1. The difference frequency was swept from 1600 to 2000 Hz. A change of temperature from 15° to 30°C decreases the shear viscosity of the alcohol, which, in turn, changes the resonance frequency and bandwidth of the tuning fork.

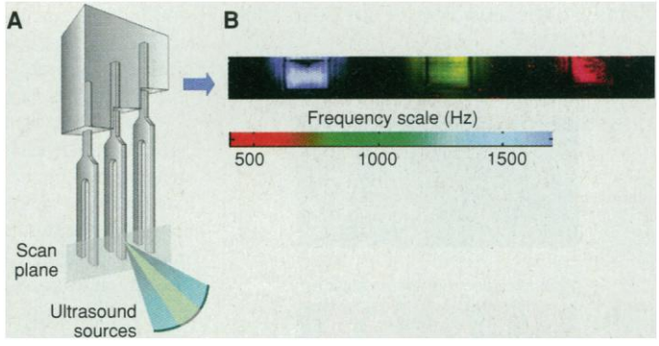

Fig. 3. Vibro-acoustic spectrogram of tuning forks. (**A**) Three tuning forks made from identical material with identical tine cross sections (lengths are different). Resonance frequencies in water are 407 Hz (right), 809 Hz (middle), and 1709 Hz (left). The forks were scanned in a water tank with the use of the system shown in Fig. 1. The scanning plane covers the front tines at the bottom part of the forks. At each position, the difference frequency was swept from 250 to 2250 Hz. The ultrasound-stimulated acoustic emission was detected with the hydrophone and filtered by three overlapping bandpass filters with frequencies centered at 500, 1000, and 1500 kHz, respectively. (**B**) Color acoustic spectrogram of the forks. The outputs of the bandpass filters were used to produce the red, green, and blue image components. This image displays two characteristics of the object: shape and frequency response. The color associated with each fork indicates its resonance frequency, which can be deduced from the frequency scale.

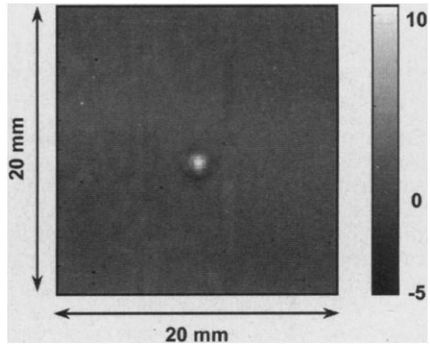

Fig. 4. Image of ultrasonically stimulated acoustic emission amplitude from a 380-μm-diameter glass bead placed on a thin latex sheet. The latex surface was scanned at 0.2-mm increments in each direction. The difference frequency was fixed at 7.3 kHz. The amplitude of the acoustic emission of the bead (in relative units) is shown in gray scale. The latex sheet is almost transparent to the imaging system. The glass bead, however, presents a large acoustic impedance discontinuity, resulting in significant oscillatory radiation force. The magnitude of the radiation force gives rise to large-amplitude acoustic emission, thus yielding a high-contrast image of the bead. The image reveals a system resolution of about 700 μm. The confocal beam geometry leads to a negative-amplitude ring around the bright, positive central spot. This effect produces edge enhancement, as seen on artery walls in Fig. 5.

Calcifications within the arteries produced distinctive amplitude and phase values when compared to the normal arterial walls (Fig. 5). The phase of the oscillation of driven mechanical systems relative to the driving force depends on the ratio of mass to stiffness (*14*). Calcified regions of the diseased artery, identified by an x-ray of the sample, produced phase shifts in acoustic emission completely different from that of the noncalcified, and thus softer or less dense, regions. The amplitude images are highly detailed and exhibit variations in acoustic emission from both calcified and uncalcified regions of the diseased artery. These differences are caused by variations in the product of the reflection properties d_r and the effective mechanical vibration admittance properties $Q(\Delta\omega)$ of the tissue. Thus, vibro-acoustic spectrography is similar to conventional pulse-echo ultrasound imaging, which is sensitive to the ultrasonic parameters of the object, but has the advantage of also being sensitive to the mechanical admittance $Q(\Delta\omega)$ at low frequencies.

Motion induced by ultrasound and measured with ultrasound pulse echo has been used previously to study "hardness" (*15*). However, the sensitivity of ultrasound pulse echo to motion at common ultrasound frequencies is limited to several micrometers. The advantage of ultrasound-stimulated vibro-acoustic emission is its high displacement sensitivity. Cyclic displacement of 100 nm at 10 kHz produces an acoustic intensity of about 3.0×10^{-3} W/cm^2. Hydrophones similar to the one used in these experiments are sensitive to as little as 10^{-15} W/cm^2 and, therefore, can detect very small cyclic displacements. For example, the hydrophone detected an acoustic pressure of about 15×10^{-3} Pa at a distance of 5 cm from the glass bead shown in Fig. 4. Under the assumption of isotropic vibration, this pressure would be produced by a similarly sized sphere vibrating with a displacement amplitude of about 6 nm. The method will be more sensitive for higher frequency sound because acoustic power is proportional to the square of frequency for constant displacement amplitude. The practical upper limits for the difference frequency produced with modern ultrasound transducers is about equal to their bandwidth. For modern transducers, this value is 80% or more of the central frequency of the transducer. For experiments like those we conducted, emission frequency well in excess of 1 MHz could be produced. The lower limit on the frequency of radiation pressure is zero, that is, static pressure.

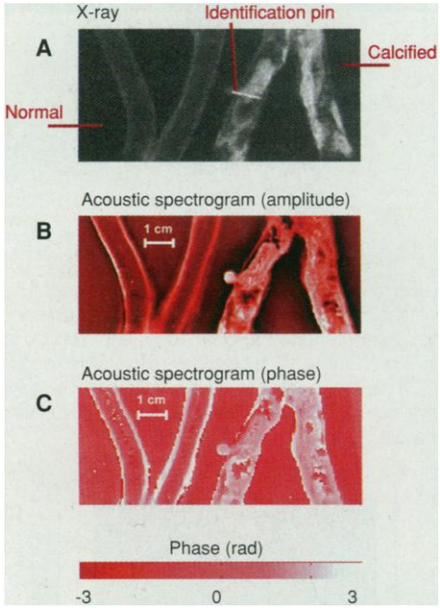

Fig. 5. Vibro-acoustic spectrography of excised human iliac arteries. (**A**) X-ray image of normal (left) and calcified (right) excised human iliac arteries obtained from a 35-year-old woman and a 67-year-old man, respectively. Bright areas indicate calcifications. (**B**) Vibro-acoustic spectrogram amplitude image at a fixed difference frequency of 6 kHz. Calcification details appear bright, whereas the arterial walls are dim. (**C**) Phase image. Calcified regions produce acoustic emission of different phase with respect to regions of the tissue having little calcification, as indicated by the x-ray.

Ultrasound-stimulated vibro-acoustic spectrography has potential applications in at least two general areas. The first is nondestructive evaluation of materials, where material characteristics and structural flaws can be identified by measuring changes in the mechanical response to vibration at a point. The object under test could be remotely vibrated, for instance, by beams propagating and interfering in either water or air, or beams propagating within the object could be used to produce acoustic emission from flaws. For medical imaging and detection, the technique appears particularly suitable for noninvasive detection of hard tissue inclusions, such as the imaging of arteries with calcification, detection of breast microcalcifications, visualization of hard tumors, and detection of foreign objects. The stiffness of soft tissues is related to their composition (for example, relative values of fibrotic content), and its change is often related to pathology or therapy. In conventional palpation, physicians estimate tissue stiffness by feeling with the fingers. Because changes of stiffness alter the vibration frequency response or damping of tissue, the present method can potentially provide a noninvasive, remote, high-resolution "palpation" technique that can reach small abnormalities that are otherwise untouchable by conventional methods.

REFERENCES AND NOTES

1. J. Maynard, *Phys. Today* **49**, 26 (January 1996).
2. R. Muthupillai *et al.*, *Science* **269**, 1854 (1995).
3. For a review of elasticity imaging methods, see L. Gao, K. J. Parker, R. M. Lerner, S. F. Levinson, *Ultrasound Med. Biol.* **22**, 959 (1996).
4. The study of radiation force and radiation pressure dates back nearly one century, to the time of Rayleigh [Lord Rayleigh, *Philos. Mag.* **3**, 338 (1902); *ibid.* **10**, 364 (1905)]. More recent analysis of the theory and explanation of the physical significance of the mathematics can be found in G. R. Torr, *Am. J. Phys.* **52**, 402 (1984). Critical and historical reviews on radiation force and radiation pressure are presented in B-T. Chu and R. E. Apfel, *J. Acoust. Soc. Am.* **72**, 1673 (1982) and R. E. Beyer, *ibid.* **63**, 1025 (1978). Some recent analysis of radiation force and pressure in attenuating medium (which may be applicable to biological tissues) are presented in O. V. Rudenko, A. P. Sarvazyan, S. Y. Emelianov, *J. Acoust. Soc. Am.* **99**, 2791 (1996) and Z.-Y. Jiang and J. F. Greenleaf, *ibid.* **100**, 741 (1996).
5. P. J. Westervelt, *J. Acoust. Soc. Am.* **23**, 312 (1951).
6. The complex drag coefficient due to radiation pressure is defined for unit energy density of the incident wave and can be written as (*5*)

$$d_r = \frac{1}{S}(\Pi_a + \Pi_s - \int\gamma\cos\beta dS) - \frac{j}{S}\int\gamma\sin\beta dS \quad (4)$$

where Π_a and Π_s are the total absorbed and scattered powers, respectively; γ is the scattered intensity (π_a, π_s, and γ are expressed per unit incident intensity); β is the angle between the incident and scattered intensities; s is the projected area of the object; and dS is the area element. The real and imaginary parts represent the components of the force parallel and perpendicular to, respectively, the incident field momentum. In our treatment, we assume a planar object normal to the beam axis; hence, d_r is real, and the force has only a normal component to the object surface.
7. The term "acoustic emission" is used here to describe the acoustic field in response to a cyclic vibration of the object and should not be confused with similar terminology used in the field of nondestructive testing of materials or in opto-acoustic imaging context, where it is used to describe the acoustic field resulting from structural deformation, cracking, or thermal expansion of the object. We note a fundamental difference between the method we present and that of opto-acoustic imaging. In ultrasound-stimulated vibro-acoustic spectrography, the ultrasound energy is converted directly to low-frequency acoustic energy by the object, whereas the opto-acoustic method relies on the conversion of light energy to heat, causing acoustic emission in response to rapid thermal expansion of the object.
8. Modulation of a single beam with the use of a focused transducer driven by an amplitude-modulated signal results in a field that is not spatially confined, producing a radiation force on any object (including the transducer itself) that happens to be in the beam path. The use of two single-frequency beams is advantageous because field modulation occurs only in a confined region, the size of which is controlled by the intersection of the two beams.
9. We define the short-term time average of an arbitrary function of time $f(t)$ around time instance t as

$$\langle f(t)\rangle_T = \frac{1}{T}\int_{-T/2}^{T/2} f(\tau - t)d\tau \quad (5)$$

The long-term time average is obtained when $T \to \infty$. To compute the short-term time average of the acoustic energy density relevant to acoustic emission at $\Delta\omega$, we choose T longer than the ultrasound wave period but much shorter than the acoustic wave period, that is, $2\pi/\omega_2 \ll T \ll 2\pi/\Delta\omega$.
10. In Eq. 2, $H(\Delta\omega)$ can be position-invariant if the geometry of the propagation medium remains unchanged during the scan. In our experiments, we minimized position dependency by fixing the position of the transducer relative to the hydrophone and moving, instead, the object in raster-scanning motion.
11. Changing $\Delta\omega$ by shifting the frequency of the ultrasound

beams does not change the beam amplitude because $\Delta\omega$ is a small fraction of the bandwidth of typical ultrasound transducers. For instance, the bandwidth of the ultrasound transducer may be greater than 1 MHz, whereas $\Delta\omega$ might be around 10 kHz.
12. M. R. Fisch, R. P. Moeller, E. F. Carome, *J. Acoust. Soc. Am.* **60**, 623 (1976).
13. D. R. Lide, Ed., *CRC Handbook of Chemistry and Physics* (CRC Press, Boca Raton, FL, ed. 72, 1991), pp. 6–158.
14. P. M. Morse and K. U. Ingard, *Theoretical Acoustics* (McGraw-Hill, New York, 1968).
15. T. Sugimoto, S. Ueha, K. Itoh, in *1990 IEEE Ultrasonics Symposium Proceedings*, B. R. McAvoy, Ed. (Institute of Electrical and Electronic Engineers, New York, 1990), vol. 3, p. 1377.

10 November 1997; accepted 17 February 1998

Flower-Associated Brachycera Flies as Fossil Evidence for Jurassic Angiosperm Origins

Dong Ren

Pollinating insects played a decisive role in the origin and early evolution of the angiosperms. Pollinating orthorrhaphous Brachycera fossils (short-horned flies) collected from Late Jurassic rocks in Liaoning Province of northeast China provide evidence for a pre-Cretaceous origin of angiosperms. Functional morphology and comparison with modern confamilial taxa show that the orthorrhaphous Brachycera were some of the most ancient pollinators. These data thus imply that angiosperms originated during the Late Jurassic and were represented by at least two floral types.

The ancestors and time of appearance of angiosperms remain obscure (*1–5*). The earliest fossil evidence of nectar secretory tissue is provided by the Santonian-Campanian flowers from Sweden (*6*). The oldest angiosperm pollen grains have been found in Israel, in strata of Early Cretaceous time (Late Valanginian to Early Hauterivian) (*7*). The earliest recognized angiosperm inflorescences have been recovered from rocks of Late Hauterivian Age at Jixi, China (*8*).

The origin and early evolution of flowering plants are probably related to the coevolution of insect pollinators (*9–11*). Cretaceous and Tertiary flower-visiting insects were diverse and include an impressive variety of Coleoptera (beetles), Diptera (true flies), Lepidoptera (moths), Hymenoptera (wasps and bees), and other less diverse taxa, such as Thysanoptera (thrips). Some highly faithful pollinators such as butterflies and cyclorraphan flies appeared in the middle Tertiary (*12*). Few pre-Cretaceous pollinating insects are known. Small insects, especially flies and parasitoid wasps, may have been important then and thus in the origin and evolution of angiosperm pollination (*13*). Here I describe Late Jurassic pollinating orthorrhaphous Brachycera with well-preserved nectaring mouthparts.

Early pollinating insects have long tubular mouthparts designed for feeding on or extracting nectar from long tubular flowers (*9–11*). Other examples of Jurassic insects having this type of mouthpart include nemonychid weevils, which probably fed on bennettitaleans or cycads (*14*), and a monotrysian Lepidopteran with a siphonate proboscis (*15, 16*).

I collected the fossil Brachycera at a locality near Beipiao City, Liaoning Province, China, from nonmarine sedimentary rocks of the Yixian Formation (*17*). These rocks contain abdundant remains of insects (*18, 19*), fishes, conchostracans, reptiles, birds, and mammals of Late Jurassic (approximately Tithonian) age (*20*).

Extant Brachycera comprise a wide variety of flower visitors (*9, 10*). Most orthorrhaphous Brachycera feed on flowers as adults. The new fossil orthorrhaphous Brachycera (*19*) include deer flies (Pangoniinae of Tabanidae), flower-loving flies (Apioceridae), and tangleveined flies (Nemestrinidae).

Most extant pangoniines are exclusively flower feeders (*21*). They often hover over flowers on the borders of dense vegetation (*9, 10*). Both males and females subsist on nectar and on the juice of flowers. The female proboscis of some species is flexible and suitable only for imbibation of nectar (*22, 23*), and is three or four times the length of the body. One of the Jurassic fossils, described as *Palaepangonius eupterus* Ren, 1998, includes a complete body and an associated well-developed long proboscis (Fig. 1) (*19*). These fossils provide direct evidence for the mid-Mesozoic diversification within Tabanidae of subclades with nectaring mouthparts. *Palaepangonius* not only provides evidence for the extraction of nectar from flowers or flowerlike structures but also demostrates that the Pangoniinae have existed since the Late Jurassic. Another brachyceran clade, the Nemestrinidae, are important pollinators of flowers (*9, 10*). Modern members are often collected when feeding on blossoms or hovering over them while imbibing nectar (*24*). Many Late Juriassic examples were collected and were described as *Protonemestrius jurassicus* Ren, 1998. These had a proboscis about 5.2 mm long, which would have been especially suitable for visiting long tubular flowers (Fig. 2). *Florinemestrius pulcherrimus* was also an important flower visitor. Its long stout proboscis seems to have been suited to extracting nectar from open or short tubular flowers (Fig. 3). Similar proboscides have been reported from the Late Jurassic of Karatau, Kazakhstan (*25*).

A representative of the stem group of the Apioceridae has also been found (Fig. 4) and called *Protapiocera megista* Ren, 1998. Its body bears dense hairs, a feature used in

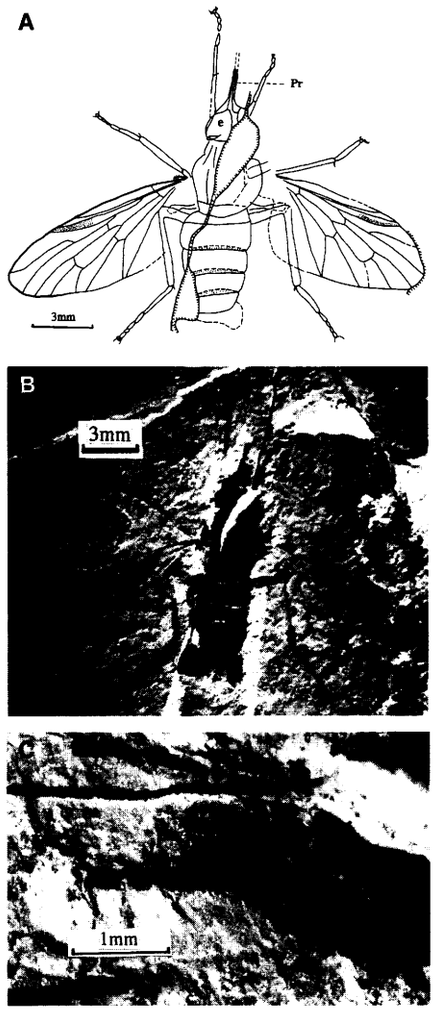

Fig. 1. *Palaepangonius eupterus* Ren, 1998. (**A**) Camera lucida drawing of specimen LB97017. (**B**) Photograph of body, LB97017. (**C**) Photograph of proboscis, LB97017. Abbreviations: e, compound eye; Pr, proboscis.

National Geological Museum of China, Xisi, Beijing 100034, China.